Solid state reduction of nickelate thin films

Wenzheng Wei [1,*] Kidae Shin [2] Hawoong Hong [3] Yeongjae Shin [1] Arashdeep Singh Thind [4] Yingjie Yang [4] Robert F. Klie [4] Frederick J. Walker [1] and Charles H. Ahn [1,2,5]

[1]*Department of Applied Physics, Yale University, New Haven, Connecticut 06520, USA*
[2]*Department of Physics, Yale University, New Haven, Connecticut 06520, USA*
[3]*Advanced Photon Source, Argonne National Laboratory, Argonne, Illinois 60439, USA*
[4]*Department of Physics, University of Illinois Chicago, Chicago, Illinois 60607, USA*
[5]*Department of Mechanical Engineering and Materials Science, Yale University, New Haven, Connecticut 06520, USA*

(Received 8 August 2022; accepted 12 January 2023; published 31 January 2023)

The square-planar nickelates are a class of superconductors analogous to the cuprates and promise to provide insight into the pairing mechanism in high-temperature superconducting oxides. The parent phase of doped superconducting films is $NdNiO_2$, which is prepared by reducing 3^+ Ni in $NdNiO_3$ films. In this paper, we develop an ultrahigh vacuum reduction method using aluminum deposited on top of the 3^+ nickelates and monitor the reduction process in real time through *in situ* crystal truncation rod measurements and diffraction x-ray absorption near edge spectroscopy measurements across the Ni *K* edge. We establish a relation between Ni valence and the lattice constant of $NdNiO_{3-x}$ and show that the process can precisely control the oxygen content in the films. Finally, we extend the reduction process to quintuple square-planar nickelates.

DOI: 10.1103/PhysRevMaterials.7.013802

I. INTRODUCTION

The square-planar nickelates are a class of superconductors [1] analogous to the cuprates and promise to provide insight into the pairing mechanism in high-temperature superconducting oxides [2–6]. The square-planar nickelate structure consists of a NiO_2 layer sandwiched by rare-earth metal layers, achieving a Ni^{1+} valence. Experimentally, superconductivity is intrinsic to the structure, as evidenced by its presence in various square-planar nickelates fabricated with different dopants, such as $Sr:LaNiO_2$, $Sr:PrNiO_2$, $Ca:LaNiO_2$ [1,7–10], and in a reduced quintuple Ruddlesden-Popper structure $Nd_6Ni_5O_{12}$ [11]. Interestingly, all superconducting films show a nominal hole-doping level of 20% on the rare-earth site, highlighting the importance of hole doping as the key to superconducting nickelates [12].

To date, square-planar thin films are synthesized by first growing a fully oxidized nickelate parent thin film with the perovskite structure and reducing it using CaH_2 [7,13,14]. Reduction is achieved by lowering the oxygen activity in a quartz reaction ampule by scavenging residual oxygen in the tube through a reaction to $Ca(OH)_2$. Note that the decomposition temperature of the hydride is too high for hydrogen to play a role [15]. The temperature of the CaH_2 reduction process needs to be high enough for oxygen diffusion through and out of the thin film. The oxygen activity in the reaction vessel is on the order of 10^{-60} Torr, or far below what is readily achievable in a vacuum system (see Supplemental Material [16] for the estimation). Some success has been reported when thin films are annealed in ultrahigh vacuum [17] or at relatively high temperature in an oxygen-deficient atmosphere [18,19], but no vacuum-based process completely removes the apical oxygen. An important challenge of a hydride topotactic reduction process is timing an anneal at a specified temperature to control oxygen content [20] and achieve superconducting behavior [7]. If the sample is annealed too long or at too high a temperature, the reduction results in phase separation to metallic constituents [21]. An advantage of implementing an alternate reduction process is that the hydride reduction process may introduce impurities, secondary phases [22,23], and residual hydrogen, which may trigger another electron or atomic configuration [24,25].

In this paper, we introduce a process to reduce $NdNiO_3$ to $NdNiO_2$ and $Nd_6Ni_5O_{16}$ to $Nd_6Ni_5O_{12}$ using metallic aluminum to control the oxygen content in the films by varying the coverage of aluminum. In contrast to controlling the oxygen activity to change the oxygen content, we demonstrate control of the oxygen number through straightforward control of aluminum coverage. We follow the reduction process using x-ray diffraction to measure changes in both electronic and physical structure. Measurements of electronic structure changes are done using an anomalous diffraction technique to probe the near edge electronic structure [diffraction x-ray absorption near edge spectroscopy (dXANES)] and correlate the electronic structure with a lattice parameter by measuring crystal truncation rods (CTRs), both of which are measured in real time during the reduction process. These measurements are made as a function of Al surface coverage and temperature. The metal reduction method in this paper provides a pathway to synthesize square-planar nickelate thin films with reduced impurities that could be caused by the postannealing process or by using CaH_2 [21–26]. The oxygen reduction by Al layer deposition also preserves an atomically flat surface

*wenzheng.wei@yale.edu

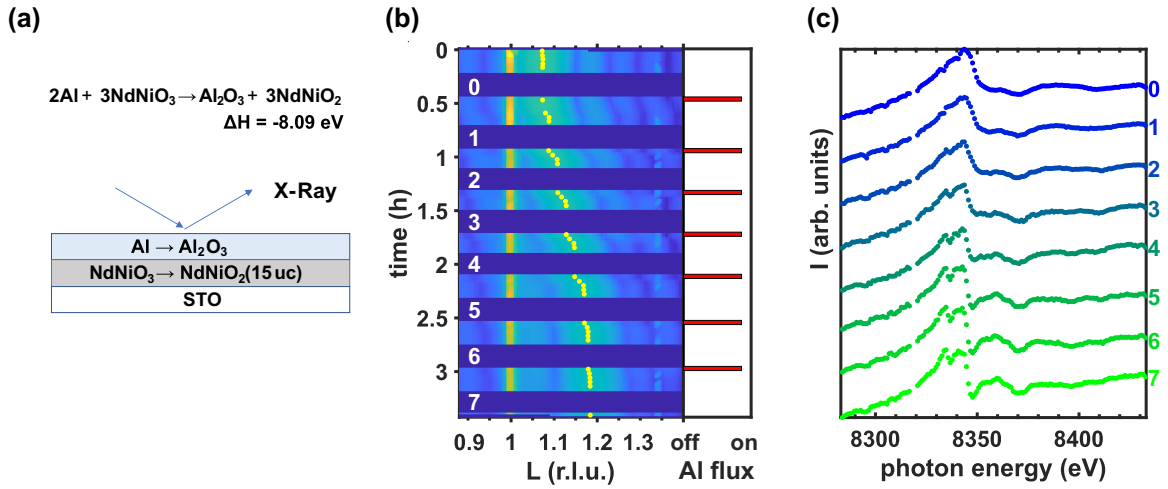

FIG. 1. *In situ* characterization during reduction. (a) Experimental diffraction geometry and *in situ* reduction reaction. The reaction shown is exothermic with a formation energy of 2.7 eV per oxygen atom removed from $NdNiO_3$. (b) and (c) Crystal truncation rod (CTR) and diffraction x-ray absorption near edge spectroscopy (dXANES) taken during a shutter-controlled reduction. (b) shows a two-dimensional plot of 37 CTR (00L) scans on a log scale on the high-temperature, shutter-controlled (HTS) reduced sample. Each slice in the bright zone is a CTR scan, with the yellow dots locating the nickelate Bragg peak. Aluminum deposition is started and stopped after 1 monolayer (ML) is deposited seven times during the HTS process. The white number indicates the total Al thickness in MLs. The nickelate Bragg position shifts from $L = 1.07$ ($c = 3.64$ Å) to $L = 1.185$ ($c = 3.30$ Å) after reduction. In each dark blue region of the plot, an energy scan of the scattered intensity is done at the nickelate Bragg position determined from the previous CTR scan. A strong anomalous scattering signal is observed as shown in (c). The labels in (c) correspond to those shown in (b) and indicate the total Al thickness in MLs.

of the film by avoiding surface roughening by thermal annealing [27], which can enable surface-sensitive physical and electronic structural analyses that could not be achieved in the conventional CaH_2 reduction method. With these advantages, this method can be used to improve understanding of the superconducting square-planar nickelates.

II. METHODS

A. $NdNiO_2$ thin film synthesis

Thin films of $NdNiO_3$ are grown to a thickness of 15 unit cells (u.c.) epitaxially on single-crystal $SrTiO_3$ (STO) (001) substrates using oxide molecular beam epitaxy (MBE). The samples are grown at 570 °C using an activated RF plasma oxygen source at a chamber pressure of 5×10^{-6} Torr. The films are subsequently taken to the *in situ* MBE-scattering chamber at the Advanced Photon Source, sector 33-ID-E, to perform both the reduction process and *in situ* measurements of structure [28]. The process for the measurements starts by annealing the films at 350 °C in 3×10^{-5} Torr of distilled ozone or oxygen ambient to obtain clean surfaces. The thin films are subsequently reduced by depositing Al at substrate temperatures of 200 and 270 °C using either a continuous or a shutter-controlled deposition process [Fig. 1(a)]. The Al flux is calibrated by a quartz crystal microbalance and set to 0.5 layer/min where 1 monolayer (ML) corresponds to an atomic density of 6.558×10^{14} cm^{-2}. The film is reduced by Al deposition in a vacuum of 1×10^{-9} Torr following the chemical reaction:

$$3NdNiO_3 + 2AI \rightarrow 3NdNiO_2 + AI_2O_3. \quad (1)$$

According to this reaction, complete oxidation of 1 ML Al reduces 1.5 u.c. of $NdNiO_3$ to $NdNiO_2$, which allows for the control of oxygen content in the film through control of Al coverage. The reaction is exothermic by 2.7 eV/oxygen or 260 kJ/mole O, as calculated using density functional theory, ensuring complete reduction of the perovskite phase (or 113) to the infinite layer nickelate (or 112) phase [29]. We also note that the per oxygen formation energy of Al_2O_3 (−5.65 eV) is larger than the enthalpy change of CaH_2 to $Ca(OH)_2$ (−4.40 eV), which has been shown to fully reduce nickelates [21,29].

B. $Nd_6Ni_5O_{12}$ thin film synthesis

Thin films of $Nd_6Ni_5O_{16}$ are synthesized on STO substrates by shutter-controlled growth following a shutter pattern of Nd-Ni-Nd-Ni-Nd-Ni-3 × Nd-2 × Ni [30] at 570 °C using an activated RF plasma oxygen source at a chamber pressure of 5×10^{-6} Torr [11,31,32]. A total of three superlattice unit cells are synthesized, and 10 ML Al are deposited for reduction.

C. *In situ* characterization of $NdNiO_{3-x}$ ($0 < x < 1$)

To follow the reaction of Eq. (1), we use an experimental sequence that consists of alternating measurements of one or more CTRs [33] followed by dXANES measurements. A dXANES measurement is performed by measuring the diffracted intensity at the nickelate (001) Bragg peak by scanning the incident x-ray energy over the Ni K edge. Because of strong changes in the scattering strength across the absorption edge, the diffracted intensity is strongly modulated in a way that measures the x-ray absorption spectra on the Ni site of the perovskite structure [34–37].

Three 15-u.c.-thick $NdNiO_3$ films are reduced and monitored with CTR and dXANES using three different reduction processes. The three processes are

(1) HTC, reduction proceeds at high temperature (270 °C) under a continuous Al flux.

(2) LTC, reduction proceeds at low temperature (200 °C) under a continuous Al flux.

(3) HTS, reduction proceeds at high temperature (270 °C) using a shutter-controlled Al flux.

For HTC and LTC, Al is deposited continuously to a final coverage of 15 ML, which is more than what is required to reduce 15-u.c.-thick films according to Eq. (1). For shutter-controlled reduction, a shutter in front of the Al source controls the deposited amount to 1 ML Al each time the shutter is opened, and a total coverage of 7 ML is achieved after reduction.

The measurement program to follow the reduction processes depends on the process. During the HTC reduction, continuous CTR scans are taken in a limited volume of reciprocal space. Each scan takes ∼150 s. During LTC reduction, continuous CTR and dXANES scans are taken alternatively. Note that, as the reduction process proceeds, the position of the nickelate Bragg reflection changes so that each dXANES measurement is measured at a different location in reciprocal space, i.e., the location of diffracted maximum in the previous CTR scan. Each CTR scan takes 150 s and dXANES takes ∼900 s. HTS reduction repeats the following processes: We start depositing Al while performing CTR scans. The Al flux is stopped after 1 ML Al is deposited in 120–140 s, while the CTR scans continue until the diffraction pattern shows negligible change for two consecutive scans. After that, dXANES at the nickel K edge is measured at the main Bragg reflection, followed by another CTR scan that confirms the diffraction pattern has not changed during the dXANES scans. The operation is repeated until the diffraction peak in CTR scans indicates the film is fully converted to $NdNiO_2$. Each repeat takes ∼30 min in total, involving 4–5 CTR scans, 1 dXANES scan, and 1 CTR scan for confirmation. Figure 1(b) shows a two-dimensional plot of diffracted intensity as a function of time and position in reciprocal space along the (00L) direction for the HTS process. Figure 1(c) shows dXANES scans that are measured during the time indicated by the dark strip in Fig. 1(b), at the location in reciprocal space indicated by the yellow dot right above each dark strip.

D. Data analysis for CTR and dXANES scans

CTR data are analyzed by fitting a thin film model that assumes that, at all stages of the process, the thin film has a homogeneous composition and an out-of-plane lattice parameter. The dXANES data analysis is performed using a self-consistent Kramers-Kronig algorithm [37,38] to obtain the imaginary part of the Ni scattering factor $f''(E)$ as a function of incident x-ray energy E across the K edge. The energy of the white line peak is calculated by fitting the region around the peak maximum; the principal component analysis (PCA) is conducted to achieve Ni valence (see Supplemental Material Fig. S1 [16] for details).

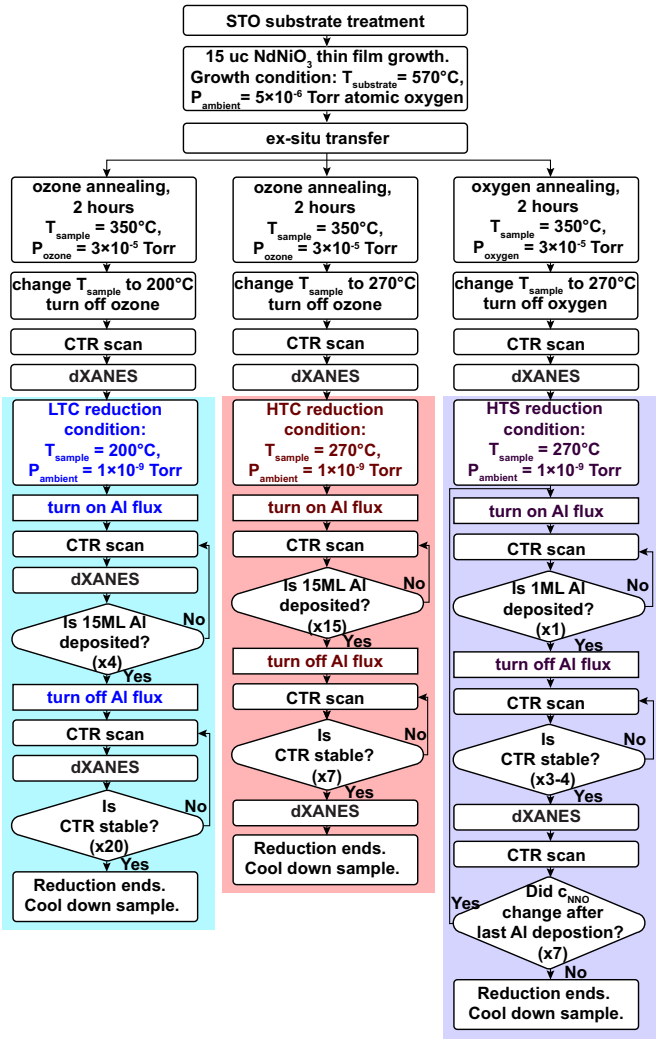

FIG. 2. Scripts describing sample preparation and characterization for the low-temperature continuous (LTC), high-temperature continuous (HTC), and high-temperature, shutter-controlled (HTS) processes. The number in each decision panel indicates the typical number of iterations before the next step.

The thin film synthesis and *in situ* characterization experimental scripts for the LTC, HTC, and HTS processes are summarized in Fig. 2.

III. RESULTS AND DISCUSSION

In situ reduction starts with a 15-u.c.-thick $NdNiO_3$ thin film after annealing, and reflection high-energy electron diffraction (RHEED) indicates a clean 2 × 2 RHEED pattern, which is consistent with oxygen octahedral rotations in the film [39] [Fig. 3(a)]. The number of diffracting nickelate crystal planes is determined from a fit of the CTR profile [Fig. 3(b)] to the period of finite thickness oscillations (see Supplemental Material Fig. S2 [16] for fitting details). As Al is deposited on the $NdNiO_3$ phase, the RHEED patterns disappear and the x-ray Bragg reflection from the nickelate moves toward larger out-of-plane momentum L [Fig. 1(b)]. The disappearance of RHEED indicates the formation of an amorphous Al_2O_3 layer, and the changes in crystal volume

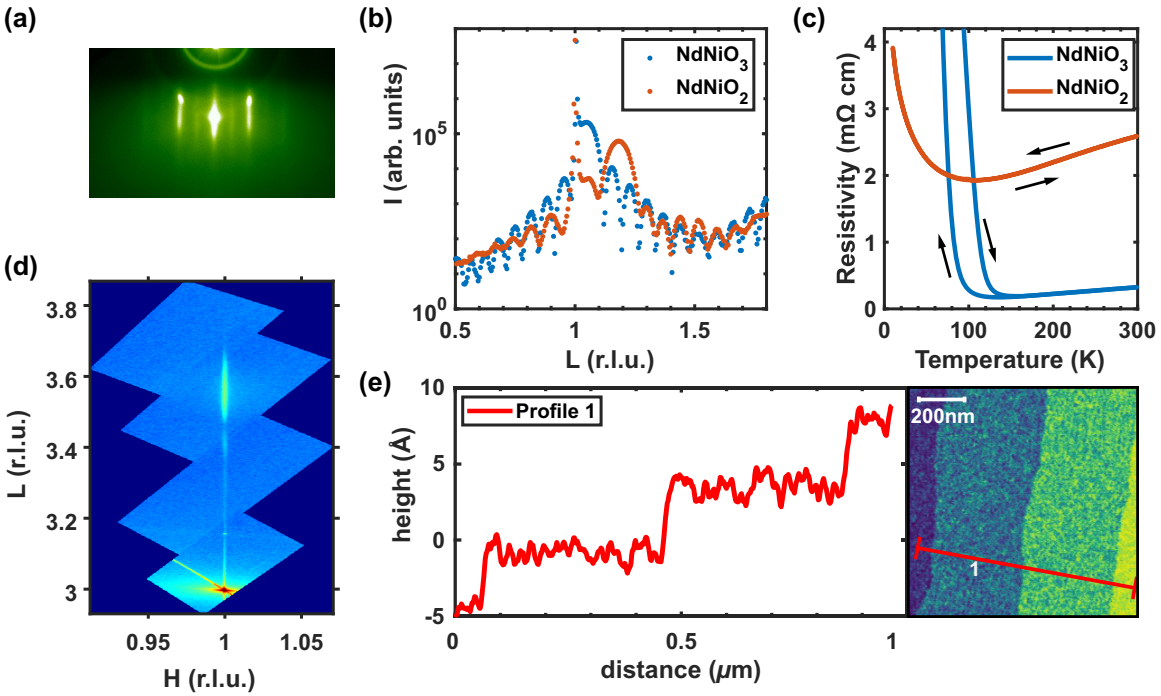

FIG. 3. Experimental characterization before and after reduction. (a) Reflection high-energy electron diffraction (RHEED) pattern of the $NdNiO_3$ thin film before reduction. (b)–(e) Characterization of $NdNiO_{3-x}$ thin films before, during, and after reduction. (b) The (00L) crystal truncation rod (CTR) scans for $NdNiO_3$ and $NdNiO_2$ thin films. The x axis is in units of STO reciprocal lattice units (r.l.u.). (c) Resistivity of 15 u.c. $NdNiO_2$ and $NdNiO_3$ thin films. Note that, for $NdNiO_2$, the resistivity measured overlaps while heating and cooling. (d) Off-specular (103) reciprocal space map (RSM) of a $NdNiO_2$ film. (e) Surface topography measured using atomic force microscopy (AFM) of an Al_2O_3-capped $NdNiO_2$ thin film.

follow the removal of oxygen in $NdNiO_3$ to fully reduced $NdNiO_2$, as deduced from a comparison of the volume at the end of the process (50.32–50.62 Å^3/u.c.) and that measured for fully reduced polycrystal $NdNiO_2$ using CaH_2 (V = 50.86 Å^3/u.c.) [7,21]. We note that this value is smaller than what can be achieved by annealing in a Mg-trapped furnace for $SmNiO_{3-x}$/LAO thin films (V = 54.49 Å^3/u.c.) [18]. Both observations are consistent with the reaction of aluminum and $NdNiO_3$ in Eq. (1) [Fig. 1(a)]. We note that this film is stable when removed to air, as evidenced by an *ex situ* reciprocal space map (RSM) measurement taken 45 d after the sample is grown [Fig. 3(d)] [40]. The RSM also shows that the in-plane lattice constant of the thin film is equal to that of the substrate, meaning that the film remains strained to the substrate after reduction.

Atomic force microscopy (AFM) images after reduction can be used to infer the homogeneity of the reduction process. In Fig. 3(e), the surface topography is shown for an Al-reduced $NdNiO_2$ film. A step-terrace structure is observed with terraces ∼500 nm wide and a step height equal to the thickness of a STO unit cell (∼0.4 nm high). The roughness (1.97 Å rms) from a 10 × 10 μm area (see Supplemental Material Fig. S3 [16] for the AFM image) is only slightly larger than half of the STO step height (1.95 Å), indicating a uniform Al_2O_3 capping layer after reduction.

The resistivity as a function of temperature for $NdNiO_2$ and $NdNiO_3$ is measured using a van der Pauw configuration and shown in Fig. 3(c). Both phases show a metal-to-insulator transition (MIT) with a transition temperature of 100 K for the 112 phase and 120 K for the 113 phase, like previous reports [14,41].

To demonstrate how the reduction process can be controlled, we analyze the CTR data during reaction and compare three different conditions used to reduce $NdNiO_3$. The most straightforward metrics to evaluate the reduction process are the lattice parameter and thickness of the crystalline phase, which can be calculated by the position and full width at half maximum (FWHM) of the nickelate Bragg peak, respectively. Results are shown in Fig. 4(a). Film reduction at low temperature (LTC) slows down more than at higher temperature (HTC) before reduction is complete: Both processes end at a lattice constant of 3.32 Å, but the LTC process takes six times longer than the HTC process. On the other hand, the HTC process using excess Al results in a significantly thinner film with lower uncertainty in film thickness. These observations indicate a slow reduction at low temperature and film degradation when excess Al is deposited. The reduction process is more precise for the shutter-controlled process (HTS), and no reduction in film thickness is observed. The limited diffraction data presented here leave open some questions. For example, how does the reduction take place? One possibility is that there is a planar phase boundary between the 113 phase and an intermediate $Nd_3Ni_3O_7$ (337) phase, as shown by Wang *et al.* [20]. Can disorder that arises from a solid solution of oxygen vacancies be measured? Such a measurement would help pin down disorder in the NiO_2 and NdO planes and its role in the superconducting behavior. The process we present here enables CTR measurements in larger volumes of

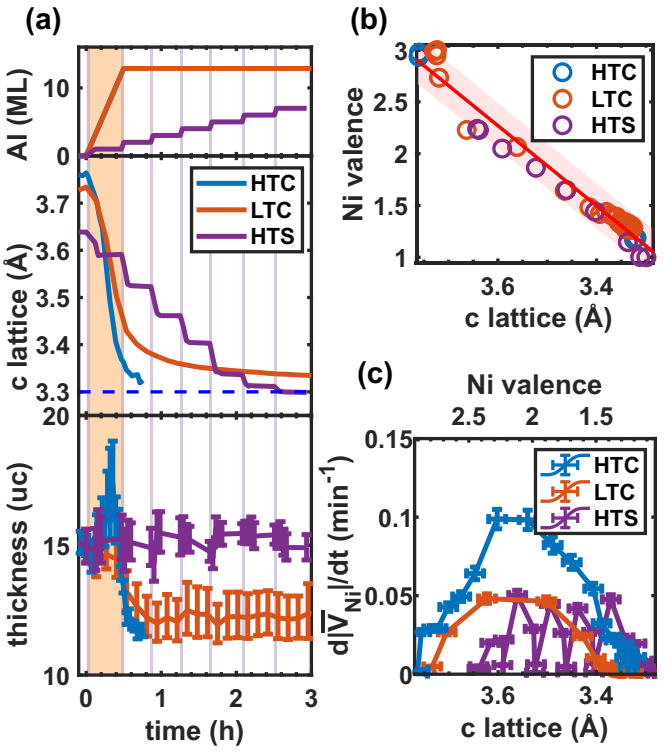

FIG. 4. Comparison of three reduction conditions. (a) follows the change of the nickelate lattice constant and thickness as a function of time and Al coverage. The light gray lines indicate when Al is being deposited during high-temperature, shutter-controlled (HTS) reduction. The film thickness is calculated by the full width at half maximum (FWHM) of diffraction peaks using the Scherrer equation (see Supplemental Material Fig. S4 [16] for details). (b) Average Ni valence $\bar{V}$ as a function of $NdNiO_2$ lattice constant. The red curve is from a linear fitting, and the patched region indicates the 95% confidence interval. (c) plots the change in rate of the average Ni valence during reduction for the three processes.

reciprocal space on *ex situ* prepared films in which the reduction process is arrested at intermediate stages by controlling the Al deposition.

We can also correlate the lattice parameter with Ni valence to characterize the electronic structure at intermediate stages as a function of vacancy content. To do this, we first determine valence using the measured dXANES at each step of the reduction process. Valence is determined from the dXANES measurements at intermediate stages using a PCA method. For the PCA, we use dXANES measurements from the as-grown $NdNiO_3$ LTC film and the dXANES measurements from the reduced HTS film for the $NdNiO_2$ standard to obtain a self-consistent picture of the valence for all films. We note that, for the as-grown film used in the HTS process, the lattice parameter measurements show that it starts out partially (30–40%) reduced by annealing in molecular oxygen but becomes fully ($> 95\%$) reduced by the HTS process. Lattice parameter measurements for the as-grown LTC film annealed in distilled ozone show that it starts fully oxidized and is only partially (80–90%) reduced after LTC reduction [Fig. 4(a)].

Once the calibration in Fig. 4(b) is done using the dXANES measurements taken during the pauses of the HTS process, we can plot the rate of change in Ni valence vs the lattice parameter [Fig. 4(c)]. Both LTC and HTC reduction processes show a parabolic rate dependence on vacancy content, which is consistent with a vacancy diffusion model in the nickelate and a temperature dependence of the diffusion constant [42]. Note that a more quantitative analysis is hindered by uncertainty in the role of the oxidation rate of the top aluminum [43]. We observe faster oxygen diffusion using the HTC process, and excess Al leads to film decomposition, as seen from the decrease of film thickness and diffracted intensity for $c < 3.4$ Å. This likely results from further reduction of $NdNiO_2$ into Nd_2O_3 and Ni (see Supplemental Material Fig. S5 [16] for evidence of film degradation). To optimize the $NdNiO_2$ film quality, we control the amount of Al and use a higher temperature. We then employ this process to determine additional details of how the reduction proceeds.

We first determine how much oxygen is removed after each layer of Al is deposited using the PCA analysis of the dXANES measurements described earlier. The results are shown in Fig. 5(a) and show that each layer of Al extracts a stoichiometric amount of oxygen from $NdNiO_{3-x}$ until the sixth layer of Al deposition. An independent characterization of oxygen content using, for example, x-ray photoemission spectroscopy, is complicated by the fact that the oxygen removed from the heterostructure ends up in amorphous Al_2O_3, thus preserving the total amount of oxygen in the composite film. By fitting the amount of deposited Al and change of Ni valence from dXANES [Fig. 5(a)], we confirm that 1 ML of Al leads to an average change of 0.211 ± 0.017 Ni valence in a 15 u.c. $NdNiO_{3-x}$ film. This implies that each Al layer deposition removes 1.5 oxygen atoms per unit cell from the $NdNiO_2$ layer, in line with the stoichiometric reaction in Eq. (1). This systematic change of oxygen content with Al coverage can be further confirmed by changes in lattice structure. Figure 5(c) shows the shift of the diffraction peak during the reduction process. A constant change in atomic structure is observed, as shown by the linear fitting of lattice constant with Al coverage [Fig. 5(a)], implying a continuous and roughly linear change of lattice constant with oxygen vacancy concentration [44].

Apart from the shift of the Ni absorption edge roughly corresponding to a change of Ni valence, we observe in the dXANES spectra a decrease in white line bandwidth and the emergence of a pre-edge peak after reduction [Fig. 5(b)] between a nickel valence of 1.4 and 1. The white line is due to a resonant transition from Ni $1s \rightarrow 4p$ [45,46], and the narrowing of the white line is attributed to a more localized $4p_\pi$ Ni orbital in $NdNiO_2$ after losing the apical oxygen atoms. The Ni K pre-edge peak lies 9 eV below the Ni white line and may be due to hybridization of the Ni $3d_{x^2-y^2}$ and O $2p$ bands and increased band localization in the direction of the incident x-ray polarization [4].

We now discuss how oxygen is removed from $NdNiO_{3-x}$ during Al reduction. There are three possibilities. The first is homogenous reduction: The oxygen occupancy in the $NdNiO_{3-x}$ film uniformly changes within the film to form randomly distributed oxygen vacancies so that the concentration of vacancies x continuously changes. The second is that the reduction process proceeds in a top-down fashion with the top layers reducing first and the layers at the $NdNiO_3$/STO interface reducing last. The third possibility is the film transforms

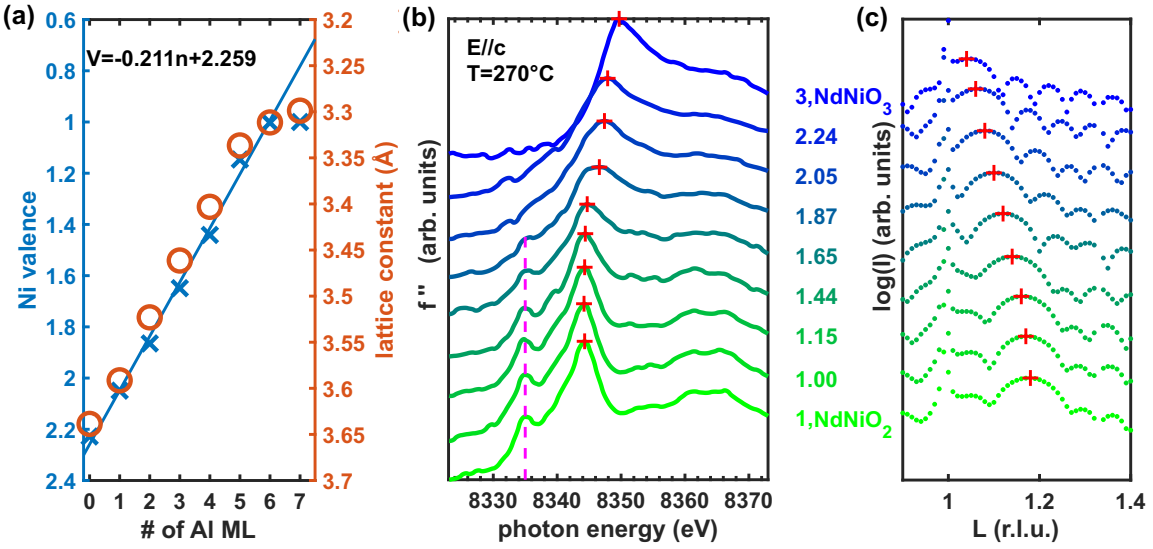

FIG. 5. Physical and electronic structure during reduction. (a) shows fits of Ni valence and c-axis lattice constant vs Al coverage ML(n). The fitting excludes the $n = 7$ point because the film is completely reduced when $n = 6$, judging from Ni valence and measured lattice parameter. (b) and (c) show diffraction x-ray absorption near edge spectroscopy (dXANES) and crystal truncation rod (CTR) data from the 15 u.c. $NdNiO_{3-x}$ thin films before and during reduction. All data are taken at $T = 270\,^{\circ}$C. The data for a $NdNiO_3$ standard is taken prior to high-temperature continuous (HTC) reduction, and the rest are measured during the high-temperature, shutter-controlled (HTS) process. The labels indicate Ni valence determined by principal component analysis (PCA) of dXANES measurements. (b) Imaginary part of the Ni anomalous scattering factor f''_{Ni} across the K edge, taken at the corresponding diffraction peak marked in (c). The white line energy is marked in each curve, and the dashed lines are guides for the eye marking the energy of a pre-edge feature that grows in intensity during reduction. (c) shows CTR scans along the (00L) direction for 15 u.c. $NdNiO_{3-x}$ thin films before and during reduction. Note that the initial lattice parameter in HTS reduction is 3.64 Å, deviating from strained $NdNiO_3$, $c = 3.76$ Å.

heterogeneously in the plane with patches of $NdNiO_2$ forming in between unreduced $NdNiO_3$, and these patches grow as the reduction process proceeds. To address this question, we perform cross-sectional scanning transmission electron microscopy (STEM) on a HTS-reduced $NdNiO_{2+\delta}$ sample at an intermediate reduction stage.

Figure 6(a) shows a high-angle annular dark-field (HAADF) image of the HTS-reduced $NdNiO_2$ sample. The square-planar nickelate film has high crystallinity and grows epitaxially on the TiO_2-terminated STO substrate with a film thickness of ∼5.5 nm. Based on the intensity of HAADF, which is approximately proportional to the squared atomic number ($\sim Z^2$) [47], we can locate the Sr and Ni cations at the atomic scale, providing a depth profile of atomic structure across the $NdNiO_2$/STO interface, as shown in Fig. 6(b). The average lattice parameter along the [010] direction is strained to that of the STO substrate throughout the thickness of the $NdNiO_2$ film, as shown in Fig. 6(c). On the other hand, the average lattice constant for $NdNiO_2$ along the [001] direction is larger at the interface and starts to contract away from the interface, eventually relaxing to the value of 3.31 Å, which agrees well with the expected value of 3.30 Å (see Supplemental Material Fig. S6 [16] for comparison of lattice constants by XRD characterization). The $NdNiO_2$ film

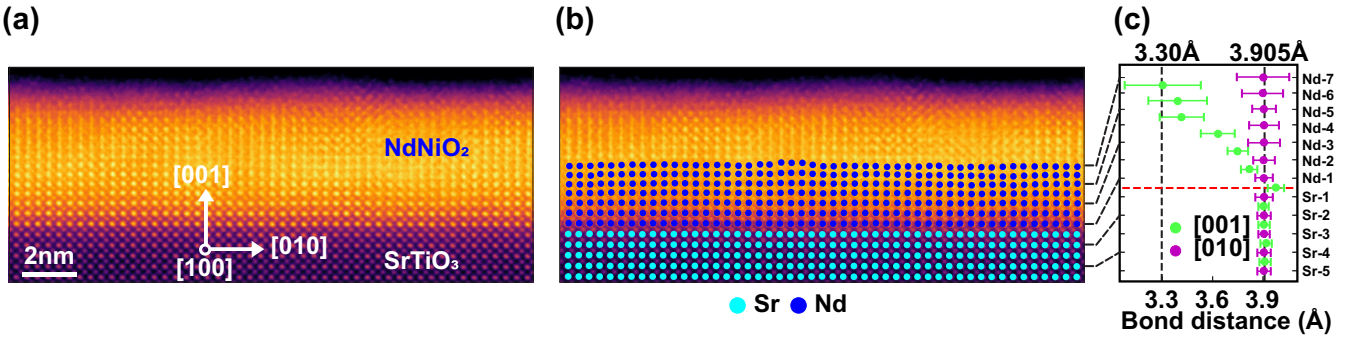

FIG. 6. Microstructure of reduction process. (a) Atomic-resolution high-angle annular dark-field (HAADF) image showing the cross-section of the $NdNiO_2$ film. The crystallographic orientations marked on the image correspond to the cubic $SrTiO_3$ structure. (b) Atomic-resolution HAADF image [same as shown in (a)] with labeled Nd and Sr atomic columns. (c) The corresponding average bond distances along [001] and [010]. The dotted red line marks the interface. The error bars correspond to the standard deviation across each atomic plane.

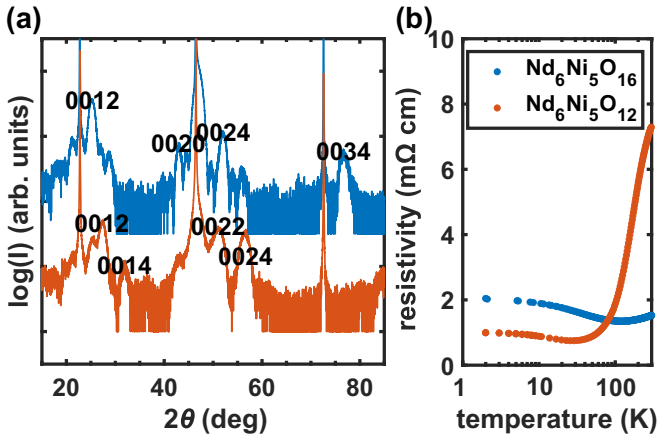

FIG. 7. (a) X-ray diffraction (XRD) of $Nd_6Ni_5O_{16}$ (top) and $Nd_6Ni_5O_{12}$ (bottom) thin films. The superlattice diffraction peaks are labeled. (b) Resistivity of 3 s.l.u.c. $Nd_6Ni_5O_{16}$ and 3 s.l.u.c. $Nd_6Ni_5O_{12}$ thin films.

approaches reduction to the square-planar phase ~6 u.c. away from the interface. This smooth change in oxygen content at this intermediate reduction stage shows that the reduction process proceeds in a top-down fashion driven by the deposition of Al (see Supplemental Material Fig. S7 [16] for additional detailed analysis of STEM results).

We now show that the reduction process can be applied to other nickelates, such as the recently discovered quintuple layer square-planar nickelate $Nd_6Ni_5O_{12}$. This nickelate has been shown to be superconducting where the additional NdO planes in a Ruddlesden-Popper structure hole dope the square-planar NiO_2 planes [11]. Here, we measure the diffraction and electrical transport characterization of Al-reduced $Nd_6Ni_5O_{12}$.

As shown in Fig. 7(a), XRD using a laboratory source shows that the starting $Nd_6Ni_5O_{16}$ phase is highly crystalline with superlattice peaks located in the expected positions for the as-grown superlattice structure. The $Nd_6Ni_5O_{16}$ is reduced by depositing 10 ML Al one monolayer at a time over 5 h at a substrate temperature of 240 °C. A highly crystalline $Nd_6Ni_5O_{12}$ phase is achieved with no change in the number of diffracting NiO_2 planes [Fig. 7(a)]. A film reduced in this way remains coherently strained and has an out-of-plane lattice parameter (39.02 Å) that can be compared with the lattice parameter of the superconducting phase (38.87 Å) [11]. The reduced $Nd_6Ni_5O_{12}$ is not superconducting [Fig. 7(b)]; instead, a MIT is observed at 28 K. This difference could be attributed to the different lattice strains, which may affect the structural and chemical defect formation or accommodation [48]. Note that the $Nd_6Ni_5O_{12}$ is under tensile stain in this paper, while in the previously reported work, $Nd_6Ni_5O_{12}$ is under compressive strain. Dimensional confinement is another possible reason for the difference in electronic properties, where the thickness of the $Nd_6Ni_5O_{12}$ film in this paper is about the same as the previously reported superconducting coherence length [11]. Additional work on $Nd_6Ni_5O_{12}$ thin films using the reduction method presented here promises to provide insights into the exotic electronic properties of this system.

IV. CONCLUSIONS

We show an alternate method for the reduction of nickelates that operates by controlling the oxygen number in the film using a straightforward tuning of Al coverage. We also show how the gradual removal of apical oxygen atoms results in a gradual structural transition from $NdNiO_3$ to $NdNiO_2$. With this process, we synthesize the $Nd_6Ni_5O_{12}$ system on STO substrates. The metal reduction method of nickelates promises additional directions. The metal reduction process is free from the use of CaH_2 and postannealing, reducing the possible impurities inside the films, such as thermally activated structural defects or residual hydrogen. The whole reduction procedure can be achieved *in vacuo* and preserves atomically flat surfaces, enabling surface-sensitive electronic structure characterization, such as angle-resolved photoelectron spectroscopy and scanning tunneling electron microscopy, of the square-planar nickelates, which has not been achieved with the conventional CaH_2 annealing method. In addition, by controlling the Al coverage, this method may lead to systematic studies of superconducting properties as a function of oxygen doping, which has been relatively less explored. In summary, the metal reduction of nickelate thin films introduced in this paper will provide a pathway to improve the understanding of superconducting square-planar nickelates.

ACKNOWLEDGMENTS

The authors acknowledge discussions with Y. He and S. Ismail-Beigi. Work at Yale was supported by the U.S. Department of Energy (DOE), Office of Science, Office of Basic Energy Sciences, under Award No. DE-SC0019211. This research used resources of the Advanced Photon Source, a DOE Office of Science User Facility, operated for the DOE Office of Science by Argonne National Laboratory under Contract No. DE-AC02-06CH11357. R.F.K. acknowledges support from the National Science Foundation (NSF; Grant No. DMR-1831406). The acquisition and upgrade of the UIC JEOL JEM ARM200CF were supported by an MRI-R^2 grant (Grant No. DMR-0959470) and an MRI grant (Grant No. DMR-1626065) from NSF.

[1] D. Li, K. Lee, B. Y. Wang, M. Osada, S. Crossley, H. R. Lee, Y. Cui, Y. Hikita, and H. Y. Hwang, Nature (London) **572**, 624 (2019).

[2] M. Kitatani, L. Si, O. Janson, R. Arita, Z. Zhong, and K. Held, npj Quantum Mater. **5**, 59 (2020).

[3] W. E. Pickett, Nat. Rev. Phys. **3**, 7 (2020).

[4] J. Karp, A. Hampel, and A. J. Millis, Phys. Rev. B **105**, 205131 (2022).

[5] H. Sakakibara, H. Usui, K. Suzuki, T. Kotani, H. Aoki, and K. Kuroki, Phys. Rev. Lett. **125**, 077003 (2020).

[6] M. Klett, T. Schwemmer, S. Wolf, X. Wu, D. Riegler, A. Dittmaier, D. Di Sante, G. Li, W. Hanke, S. Rachel *et al.*, Phys. Rev. B **104**, L100502 (2021).

[7] K. Lee, B. H. Goodge, D. F. Li, M. Osada, B. Y. Wang, Y. Cui, L. F. Kourkoutis, and H. Y. Hwang, APL Mater. **8**, 041107 (2020).

[8] Hu Zhang, L. Jin, S. Wang, B. Xi, X. Shi, F. Ye, and J.-W. Mei, Phys. Rev. Res. **2**, 013214 (2020).

[9] X.-R. Zhou, Z.-X. Feng, P.-X. Qin, H. Yan, X.-N. Wang, P. Nie, H.-J. Wu, X. Zhang, H.-Y. Chen, Z.-A. Meng *et al.*, Rare Met. **40**, 2847 (2021).

[10] Q. Gao, Y. C. Zhao, X. J. Zhou, and Z. H. Zhu, Chin. Phys. Lett. **38**, 077401 (2021).

[11] G. A. Pan, D. Ferenc Segedin, H. LaBollita, Q. Song, E. M. Nica, B. H. Goodge, A. T. Pierce, S. Doyle, S. Novakov, D. C. Carrizales *et al.*, Nat. Mater. **21**, 160 (2022).

[12] J. F. Mitchell, Front. Phys. **9**, 813483 (2021).

[13] P. Puphal, Y.-M. Wu, K. Fürsich, H. Lee, M. Pakdaman, J. A. N. Bruin, J. Nuss, Y. E. Suyolcu, P. A. van Aken, B. Keimer *et al.*, Sci. Adv. **7**, eab18091 (2021).

[14] S. Zeng, C. S. Tang, X. Yin, C. Li, M. Li, Z. Huang, J. Hu, W. Liu, G. J. Omar, H. Jani *et al.*, Phys. Rev. Lett. **125**, 147003 (2020).

[15] R. Kalamkar, V. Yakkundi, and A. Gangal, Int. J. Hydrogen Energy **45**, 30792 (2020).

[16] See Supplemental Material at http://link.aps.org/supplemental/10.1103/PhysRevMaterials.7.013802 for supporting details on thermodynamical analysis, diffraction-based experimental data analysis and *ex situ* characterization.

[17] X.-R. Zhou, Z.-X. Feng, P.-X. Qin, H. Yan, S. Hu, H.-X. Guo, X.-N. Wang, H.-J. Wu, X. Zhang, H.-Y. Chen *et al.*, Rare Met. **39**, 368 (2020).

[18] J. Li, R. J. Green, Z. Zhang, R. Sutarto, J. T. Sadowski, Z. Zhu, G. Zhang, D. Zhou, Y. Sun, F. He *et al.*, Phys. Rev. Lett. **126**, 187602 (2021).

[19] G. Koren, A. Eyal, L. Iomin, and Y. Nitzav, Materials (Basel) **14**, 7689 (2021).

[20] B. X. Wang, H. Zheng, E. Krivyakina, O. Chmaissem, P. P. Lopes, J. W. Lynn, L. C. Gallington, Y. Ren, S. Rosenkranz, J. F. Mitchell *et al.*, Phys. Rev. Mater. **4**, 084409 (2020).

[21] M. A. Hayward and J. Rosseinsky, Solid State Sci. **5**, 839 (2003).

[22] B. H. Goodge, B. Geisler, K. Lee, M. Osada, B. Y. Wang, D. Li, H. Y. Hwang, R. Pentcheva, and L. F. Kourkoutis, arXiv:2201.03613 (2022).

[23] G. Krieger, L. Martinelli, S. Zeng, L. E. Chow, K. Kummer, R. Arpaia, M. Moretti Sala, N. B. Brookes, A. Ariando, N. Viart *et al.*, Phys. Rev. Lett. **129**, 027002 (2022).

[24] N. Kitamine, M. Ochi, and K. Kuroki, Phys. Rev. Res. **2**, 042032(R) (2020).

[25] T. Onozuka, A. Chikamatsu, T. Katayama, T. Fukumura, and T. Hasegawa, Dalton Trans. **45**, 12114 (2016).

[26] G. Krieger, A. Raji, L. Schlur, G. Versini, C. Bouillet, M. Lenertz, J. Robert, A. Gloter, N. Viart, and D. Preziosi, J. Phys. D: Appl. Phys. **56**, 024003 (2022).

[27] J. Sengupta, R. K. Sahoo, and C. D. Mukherjee, Mater. Lett. **83**, 84 (2012).

[28] H. Hong, Z. Wu, T. C. Chiang, P. Zschack, and H. Chen, Rev. Sci. Instrum. **73**, 1720 (2002).

[29] A. Jain, S. P. Ong, G. Hautier, W. Chen, W. D. Richards, S. Dacek, S. Cholia, D. Gunter, D. Skinner, G. Ceder *et al.*, APL Mater. **1**, 011002 (2013).

[30] Y. F. Nie, Y. Zhu, C. H. Lee, L. F. Kourkoutis, J. A. Mundy, J. Junquera, P. Ghosez, D. J. Baek, S. Sung, X. X. Xi *et al.*, Nat. Commun. **5**, 4530 (2014).

[31] Z. Li, W. Guo, T. T. Zhang, J. H. Song, T. Y. Gao, Z. B. Gu, and Y. F. Nie, APL Mater. **8**, 091112 (2020).

[32] D. Zhao, Y. B. Zhou, Y. Fu, L. Wang, X. F. Zhou, H. Cheng, J. Li, D. W. Song, S. J. Li, B. L. Kang *et al.*, Phys. Rev. Lett. **126**, 197001 (2021).

[33] A. S. Disa, F. J. Walker, and C. H. Ahn, Adv. Mater. Interfaces **7**, 1901772 (2020).

[34] H. Stragier, J. O. Cross, J. J. Rehr, L. B. Sorensen, C. E. Bouldin, and J. C. Woicik, Phys. Rev. Lett. **69**, 3064 (1992).

[35] F. J. Walker and D. Specht, in *Resonant Anomalous Scattering, Theory and Applications*, edited by G. Materlik, C. J. Sparks, and K. Fischer (North-Holland, Amsterdam, 1994), p. 365.

[36] E. D. Specht and J. Walker, Phys. Rev. B **47**, 13743 (1993).

[37] C. Lau, N. G. Combs, E. Karapetrova, J. Jiang, S. Stemmer, C. H. Ahn, and F. J. Walker, J. Vac. Sci. Technol. A **40**, 013411 (2022).

[38] J. O. Cross, W. T. Elam, J. C. Woicik, and L. B. Sorensen, J. Synchrotron Radiat. **6**, 335 (1999).

[39] W. Sun, Y. Li, X. Cai, J. Yang, W. Guo, Z. Gu, Ye Zhu, and Y. Nie, Phys. Rev. B **104**, 184518 (2021).

[40] X. Ding, S. Shen, H. Leng, M. Xu, Y. Zhao, J. Zhao, X. Sui, X. Wu, H. Xiao, X. Zu *et al.*, Sci. China Phys., Mech. Astron. **65**, 267411 (2022).

[41] Y.-T. Hsu, B. Yang Wang, M. Berben, D. Li, K. Lee, C. Duffy, T. Ottenbros, W. Jin Kim, M. Osada, S. Wiedmann *et al.*, Phys. Rev. Res. **3**, L042015 (2021).

[42] M. G. C. Cox, B. McEnaney, and V. D. Scott, Philos. Mag. **26**, 839 (1972).

[43] L. P. H. Jeurgens, W. G. Sloof, F. D. Tichelaar, and E. J. Mittemeijer, J. Appl. Phys. **92**, 1649 (2002).

[44] J. Ye and Nakamura, Phys. Rev. B **48**, 7554 (1993).

[45] C. X. Li, M. Pompa, A. C. Castellano, S. Dellalonga, and A. Bianconi, Physica C **175**, 369 (1991).

[46] W. Gu, H. Wang, and K. Wang, Dalton Trans. **43**, 6406 (2014).

[47] S. J. Pennycook and D. E. Jesson, Ultramicroscopy **37**, 14 (1991).

[48] N. M. Dawley, B. H. Goodge, W. Egger, M. R. Barone, L. F. Kourkoutis, D. J. Keeble, and D. G. Schlom, Appl. Phys. Lett. **117**, 062901 (2020).